JOURNAL OF GEOPHYSICAL RESEARCH, VOL. 111, A10S16, doi:10.1029/2005JA011495, 2006

Click Here for Full Article

Thermospheric density 2002–2004: TIMED/GUVI dayside limb observations and satellite drag

J. T. Emmert,[1] R. R. Meier,[2] J. M. Picone,[1] J. L. Lean,[1] and A. B. Christensen[3]

Received 25 October 2005; revised 26 January 2006; accepted 30 January 2006; published 24 August 2006.

[1] We use TIMED/GUVI dayside limb observations of thermospheric far ultraviolet (FUV) dayglow to infer height profiles of total mass density during the period 2002–2004. We compare these data with total mass density derived from drag-induced changes in the orbits of satellites with perigee heights ranging from 200 to 600 km. To accommodate sampling differences, we compute the ratio of observed total mass density, filtered on a 3-day timescale, to that predicted by the NRLMSISE-00 empirical model. The GUVI densities are in good agreement with the orbit-derived densities in the 300–500 km range, where the correlation of the two independent measurements is ~0.68 and the relative bias is less than 5%, which is within the absolute uncertainty of the drag results. Of interest is a prolonged depletion of upper thermospheric density (relative to NRLMSIS) during July 2002, when densities from both techniques were 20–35% smaller than those predicted by NRLMSIS. Our results represent the first validation of absolute densities derived from FUV limb scanning.

Citation: Emmert, J. T., R. R. Meier, J. M. Picone, J. L. Lean, and A. B. Christensen (2006), Thermospheric density 2002–2004: TIMED/GUVI dayside limb observations and satellite drag, *J. Geophys. Res.*, *111*, A10S16, doi:10.1029/2005JA011495.

1. Introduction

[2] Accurate specification of thermospheric composition is critical for applications such as orbit prediction for near-Earth satellites and ionospheric assessment and forecasting. The composition and total mass density of the thermosphere were probed between 1969 and 1985 by a variety of instruments, mostly mass spectrometers and accelerometers that made in situ measurements [e.g., *Champion and Marcos*, 1973; *Carignan et al.*, 1981]. Many of these data have been assimilated into empirical climatological models [e.g., *Hedin*, 1987; *Picone et al.*, 2002]. During the 16 years between 1985 and 2001, there were few measurements of upper thermospheric (>200 km) composition and density. Currently, however, a new generation of remote-sensing probes is being deployed to provide routine global monitoring of the thermosphere, using new techniques for accurately retrieving thermospheric composition and other key thermospheric properties from ultraviolet airglow [e.g., *Meier and Picone*, 1994].

[3] The Global Ultraviolet Imager (GUVI) on board the NASA Thermosphere Ionosphere Mesosphere Energy and Dynamics (TIMED) satellite was launched on 7 December 2001 and provides pole-to-pole imaging of the thermosphere in several far ultraviolet (FUV) spectral bands [*Christensen et al.*, 2003]. GUVI observations have been used to infer daytime column O/N_2 ratios from nadir-viewing data [e.g., *Strickland et al.*, 2004] and height profiles of O, N_2, and O_2 density from limb-viewing data. The limb profiles provide substantially more information about the state of the thermosphere than the column O/N_2 ratios but until now have not been fully validated against independent, temporally coincident data sources.

[4] Although dedicated thermospheric density probes were scarce between 1985 and 2001, the thousands of objects in near-Earth orbit effectively monitor fluctuations (on timescales of a few days) in thermospheric density via changes in the objects' orbital periods. Routine determinations of these objects' orbital trajectories constitute the only continuous record of thermospheric density spanning more than 10 years. *Emmert et al.* [2004] and *Picone et al.* [2005] presented a method for efficiently exploiting the historical orbit data to obtain total mass density. The inversion is direct and the sources of uncertainty are well characterized, the primary one being the drag coefficient, which (for a sphere) is generally known to ~5–10% accuracy [*Cook*, 1966; *Moe et al.*, 1995] and which straightforwardly scales the overall density inferred from a given object. Density derived from orbital drag provides a means to rigorously validate, for the first time, absolute density inferred from UV airglow measurements. The two techniques are completely different: one is an in situ measurement of a bulk atmospheric property, and the other is an inversion of remotely sensed radiation fields.

[5] In this paper we compare thermospheric densities derived from orbital elements (herein called orbit-derived or drag density) with temporally coincident retrievals from GUVI limb profiles during the period 2002–2004. In the

[1] E. O. Hulburt Center for Space Research, U.S. Naval Research Laboratory, Washington, DC, USA.
[2] Department of Physics and Astronomy, George Mason University, Fairfax, Virginia, USA.
[3] Northrop Grumman Space Technology, Redondo Beach, California, USA.

Copyright 2006 by the American Geophysical Union.
0148-0227/06/2005JA011495$09.00

Table 1. Near-Earth Objects Used in This Study

NORAD Catalog Number	Object Name or Description	B^{T*}, m^2/kg	Starting Date	Ending Date	Perigee Height, km	Apogee Height, km	Inclination, deg
0060	Explorer 8	0.02315	1 Jan 2002	31 Dec 2004	378–371	1006–775	49.9
0063	Tiros 2	0.01498	1 Jan 2002	31 Dec 2004	509–480	555–518	48.5
0165	Rocket body	0.05328	1 Jan 2002	31 Dec 2004	599–545	621–563	47.9
0229	Rocket body	0.05379	1 Jan 2002	9 Aug 2002	482–220	514–221	48.3
0614	Hitchhiker 1	0.01463	1 Jan 2002	31 Dec 2004	330–322	2073–1820	82.0
0750	Debris	0.06846	1 Jan 2002	31 Dec 2004	397–394	4078–3777	60.8
1370	Debris	0.11858	1 Jan 2002	17 Jan 2004	482–213	853–226	56.0
1808	Debris	0.13997	1 Jan 2002	23 Sep 2002	434–231	876–263	79.7
2016	Diapason D-1A	0.02879	1 Jan 2002	31 Dec 2004	503–502	2428–2395	34.1
2129	Rocket Body	0.04307	1 Jan 2002	10 May 2002	439–207	493–231	98.1
2153	Debris	0.03329	1 Jan 2002	31 Dec 2004	514–501	2651–2608	79.7
2611	OV1-10	0.02474	1 Jan 2002	27 Nov 2002	457–236	497–251	93.4
2622	Rocket body	0.02240	1 Jan 2002	31 Dec 2004	480–496	4508–4497	99.1
3553	Debris	0.13464	1 Jan 2002	22 Jul 2004	482–208	965–228	62.2
4221	Azur	0.02201	1 Jan 2002	31 Dec 2004	390–376	1840–1658	102.7
4330	Ohsumi	0.02634	1 Jan 2002	28 Jul 2003	306–214	1310–281	31.0
6073	Debris	0.00378	1 Jan 2002	31 Dec 2004	213–216	4987–4428	52.1
7337	Vektor	0.01140	1 Jan 2002	31 Dec 2004	391–399	1406–1332	83.0
8744	Vektor	0.01126	1 Jan 2002	31 Dec 2004	392–387	1443–1363	82.9
12138	Vektor	0.01136	1 Jan 2002	31 Dec 2004	398–409	1601–1555	83.0
12388	Vektor	0.01141	1 Jan 2002	31 Dec 2004	404–386	1578–1485	83.0
14483	Vektor	0.01147	1 Jan 2002	31 Dec 2004	405–406	1677–1615	82.9
20774	Vektor	0.01168	1 Jan 2002	31 Dec 2004	404–393	1779–1708	83.0
22875	Yug	0.00856	1 Jan 2002	5 Aug 2003	271–201	889–272	82.8
23278	Vektor	0.01168	1 Jan 2002	31 Dec 2004	401–402	1857–1806	83.0
23853	Yug	0.00889	1 Jan 2002	31 Dec 2004	293–215	1054–326	82.9
25233	SNOE	0.01734	1 Jan 2002	11 Dec 2003	470–211	499–220	97.6
26405	CHAMP	0.00514	1 Jan 2002	31 Dec 2004	397–379	444–385	87.3
26929	Starshine 3	0.01620	1 Jan 2002	19 Jan 2003	459–200	465–208	67.0
26996	Starshine 2	0.01011	1 Jan 2002	23 Apr 2002	365–201	392–209	51.6
27391	GRACE 1	0.00697	17 Mar 2002	31 Dec 2004	504–471	527–493	89.0
27392	GRACE 2	0.00693	17 Mar 2002	31 Dec 2004	504–470	527–493	89.0

following sections we describe the techniques used for inferring total mass density from each data source and for intercomparison. We then analyze the results as a function of time and altitude and perform statistical comparisons. Finally, we discuss issues raised by the comparison and modifications planned for the UV retrieval methodology that may further improve the agreement with the drag results.

2. Data and Methodology

2.1. Total Mass Density From Orbit Data

[6] We derive densities from the orbital elements of 32 objects covering the years 2002–2004. The objects were selected to cover a range of altitudes and are either spheres or compact objects of known dimensions or long-lived objects with well-characterized ballistic coefficients. The sample includes the objects used in the secular change study of *Emmert et al.* [2004], as well as a few additional objects. Table 1 summarizes the orbital characteristics and temporal coverage of each object. The orbit data for most of the objects were obtained from the Naval Space Command (NSC) archives; the Starshine data are Air Force two-line element sets (TLEs). The starting and ending dates encompass the period available for each object during 2002–2004; orbits with perigees below 200 km were not used. The Vektor (also known as Type 2) and Yug objects are Russian radar calibration spheres collectively known as Taifun satellites. The Yug and Vektor spheres are both about 2 m in diameter with a mass of about 750 kg. Yug spheres are smooth, whereas the Vektor objects are covered with solar panels and have four protruding antennae (Encyclopedia Astronautica, available at http://www.astronautix.com/) [*Bowman and Moe*, 2005].

[7] From changes in the orbital period, we derive total mass density, following the method described by *Picone et al.* [2005]. The NSC orbital elements (used in this study for all objects except Starshine 2 and 3) are similar to the TLEs, but require the use of NSC's PPT3 (Position and Partials as Functions of Time 3) analytic orbit propagator [*Schumacher and Glover*, 1995], rather than the SGP4 propagator used by the Air Force. We have found that the NSC elements yield density results that are essentially identical to those derived from TLEs.

[8] Adopting the notation used by *Picone et al.* [2005], we first derived time series of model-dependent ballistic coefficients, B^M, for each object:

$$B^M_{\Delta t}(t_{ik}) = \frac{\frac{2}{3}\mu^{2/3}[n_M(t_{ik})]^{-1/3}\Delta_{ik} n_M}{\int_{t_i}^{t_k} \rho^M \nu^3 F dt} \quad (1)$$

where $\mu = GM_\oplus$ is the gravitational parameter, n_M is the Kozai mean motion of the orbit (obtained directly from the orbital elements), i and k are the indices of a pair of element sets, ρ^M is the NRLMSISE-00 [*Picone et al.*, 2002] model density, v is the magnitude of the orbital velocity, and F is a dimensionless factor that accounts for corotating winds. The time $t_{ik} = (t_i + t_k)/2$ and Δ_{ik} is the difference operator; i.e., the kth value minus the ith value of n_M. We imposed a minimum integration time Δt of three days in performing

these computations; i.e., for each element set i, the second element set k is the earliest one satisfying the condition $t_k - t_i \geq 3$ days. The time step for the integration in equation (1) was 5 min. The resulting B^M values represent the average (over time Δt) ballistic coefficient that would be inferred assuming the model density is the same as the true density. Provided the true ballistic coefficient is constant, variations in B^M represent variations in the true atmospheric density relative to model predictions [*Picone et al.*, 2005; *Marcos et al.*, 2005].

[9] Next, we estimated the true values of the ballistic coefficients by assuming (1) the true ballistic coefficient of each object is constant over the period of study, (2) the correction to the model density is the same for objects at similar effective heights (near perigee) during concurrent time periods, and (3) the true ballistic coefficient of a single reference object is known. In this approach,

$$\frac{B_l^M(t_j)}{B_m^M(t_j)} = \frac{B_l^T}{B_m^T} \tag{2}$$

where the l and m subscripts denote a pair of objects, and B^T is the true value of the ballistic coefficient. The values on the left-hand side of equation (2) were computed using the B^M values for every possible pair of objects available within a time window centered on times t_j, and B^T for one of the objects is known a priori. This overdetermined system of equations can be linearized by taking the logarithm, and a least-squares solution for all B_l^T obtained. In computing the solution, we used a time window of 1 day and weighted each ratio by $\exp(-|h_l - h_m|/H)$, where h is the perigee height and $H = 50$ km (about 1 thermospheric scale height). Our calculation covered the time period 1996–2004, and we used Starshine 1 as the reference object, with $B^T = 0.009248$ m^2/kg (this value assumes a drag coefficient of 2.2). Note that although Starshine 1 was not in orbit during the period covered by this study (2002–2004), most of the objects in Table 1 were aloft during the Starshine 1 mission (May 1999 to February 2000). The resulting estimated true ballistic coefficients, B^T*, are given in Table 1.

[10] Finally, again following *Picone et al.* [2005], ratios of the true density to the model density were computed as

$$\left\langle \frac{\rho^T}{\rho^M} \right\rangle_{\Delta t}^{DRAG} = \frac{B_{\Delta t}^M}{B^{T*}} \cong \frac{\rho_{\Delta t}^T(t_{ik})}{\rho_{\Delta t}^M(t_{ik})} \equiv \frac{\int_{t_i}^{t_k} \rho^T v^3 F dt}{\int_{t_i}^{t_k} \rho^M v^3 F dt} \tag{3}$$

[11] The third and fourth terms in equation (3) indicate that the computed ratio is, most precisely, a ratio of weighted averages of the true and model densities along the satellite trajectory. However, since the true and modeled densities are generally the same order of magnitude, this ratio can be approximately viewed as a time-averaged model scaling factor, as indicated by the first term.

[12] The orbit-derived densities have an inherent overall uncertainty as a result of imprecise knowledge of the ballistic coefficient of the spherical calibration object (Starshine 1), since the drag coefficient of a sphere composed of a given material is known only to about 5–10% accuracy; this estimate of uncertainty is based on the expected range of values of the accommodation coefficient (a measure of energy transfer between a gas molecule and a surface) [*Cook*, 1966; *Moe et al.*, 1995]. We used a value of 2.2 for the drag coefficient of Starshine 1; the use of a lower (higher) value proportionally increases (decreases) the derived density values. Our use of a spherical calibration object to infer the average ballistic coefficients of other (generally nonspherical) objects should produce density values with long-term accuracy of about 5–10%.

2.2. Total Mass Density From GUVI Data

[13] The TIMED satellite was launched on 7 December 2001 into a 630 km circular orbit with an inclination of 74.1°. GUVI is one of four instruments on board and makes spectroradiometric measurements of Earth's FUV airglow, covering wavelengths from 115 to 180 nm. Five spectral bands are imaged simultaneously, and each instrument scan covers the Earth's disk (nadir direction) and the limb away from the solar direction. A single scan takes 15 s, covering 32 steps on the limb and 159 steps on the disk. There are ~390 limb scans per orbit. On the limb, GUVI's scanning mirror is incremented by 0.4° every 0.068 s; data are accumulated only for the final 0.034 s, to allow for damping of the mirror scan mechanism. The 32 limb steps cover tangent altitudes between about 110 and 520 km. For the retrieval of major neutral species, we combine five scans to achieve an acceptable signal-to-noise ratio. *Christensen et al.* [2003] and *Paxton et al.* [1999] illustrate the GUVI scanning geometry and provide details about the instrument and on-orbit operations.

[14] We use daytime GUVI limb profiles of the atomic oxygen 135.6 nm (OI GUVI band: 134.3–137.7 nm) and the molecular nitrogen Lyman-Birge-Hopfield short wavelength (LBHS GUVI band: 141.0–152.8 nm) emissions to derive height profiles of O, N_2, and O_2 [*Meier and Picone*, 1994; *Christensen et al.*, 2003; *Meier et al.*, 2005]. The TIMED orbit precesses at a rate such that the beta angle (the angle between the Earth-Sun vector and the orbital plane) passes through zero every 120 days. As a result, the combined ascending and descending orbital passes allow GUVI to sample all local solar times every 60 days. Because GUVI limb inversions are limited to solar zenith angles less than 80°, there are temporal gaps in the GUVI retrievals when the absolute value of the beta angle is too large (typically ~60° at the equator).

[15] The inversion procedure consists of optimally fitting a parametric forward model of the radiances to the data [*Meier and Picone*, 1994; *Christensen et al.*, 2003]; radiances from tangent heights of 110–300 km were used in this study. The neutral density component of the forward model is a scaled version of the NRLMSISE-00 model [*Picone et al.*, 2002; *Meier and Picone*, 1994]. Four parameters are used to scale the model: three altitude-independent scalars (denoted f_O, f_{N2}, and f_{O2}) of the O, N_2, and O_2 number density profiles and a scalar ($f_{F_{10.7}}$) of the solar 10.7 cm radio flux inputs ($F_{10.7}^P$, the previous day value; and $F_{10.7}^A$, the 81-day average) to accommodate departures in the true altitude profiles of the species from those of NRLMSIS. The inferred number density of each species is thus written as:

$$n_x^{GUVI}(z) = f_x n_x^{MSIS}\left(f_{F_{10.7}} F_{10.7}^P, f_{F_{10.7}} F_{10.7}^A, z\right) \tag{4}$$

where $x \in \{O, N_2, O_2\}$, z is altitude, and n_x^{MSIS} is the NRLMSIS profile of species x, evaluated using the scaled $F_{10.7}$ inputs. Equation (4) shows explicitly that in the GUVI inversions the same scaling factor $f_{F_{10.7}}$ is applied to both parameters. These four scalars, along with a scalar of the OI 135.6 nm and N_2 LBHS radiances (to accommodate calibration and/or solar irradiance offsets), are retrieved by optimally fitting each limb scan with the forward model. Although radiances above 300 km are not used in the inversion, the use of NRLMSIS (which employs a Bates-Walker profile to represent height dependence) as a forward model allows extrapolation to higher altitudes.

[16] To compute total mass densities from the GUVI measurements, we combined the contribution from the scaled O, N_2, and O_2 outputs with the NRLMSIS profiles of He, N, H, and Ar corresponding to the scaled $F_{10.7}$ inputs. The dominant species are usually O, N_2, and O_2 in the 200–600 km region covered by the drag data, but above about 550 km during solar minimum (800 km during solar max), He can be the dominant species in NRLMSIS. The ratio of the total mass density inferred from GUVI to that of NRLMSIS is then

$$\frac{\rho^{GUVI}}{\rho^{MSIS}}(z) = \frac{\sum_i n_i^{GUVI} m_i}{\sum_i n_i^{MSIS} m_i}$$

$$n_i^{GUVI} = \begin{cases} f_i n_i^{MSIS}\left(f_{F_{10.7}} F_{10.7}^P, f_{F_{10.7}} F_{10.7}^A, z\right); & i = O, O_2, N_2 \\ n_i^{MSIS}\left(f_{F_{10.7}} F_{10.7}^P, f_{F_{10.7}} F_{10.7}^A, z\right); & i = N, He, H, Ar \end{cases}$$

$$n_i^{MSIS} = n_i^{MSIS}\left(F_{10.7}^P, F_{10.7}^A, z\right) \tag{5}$$

where m_i is the particle mass of species i. Note that even though the GUVI retrievals do not include scalars for all of the NRLMSIS species, the temperature information implicit in the $F_{10.7}$ scalars ensures that the NRLMSIS height dependences of all seven species are modified consistent with the 135.6 nm and LBHS profiles.

2.3. Comparing Drag and GUVI Densities

[17] As described in section 2.1, each density ratio derived from a given orbiting object represents the average density along its trajectory, relative to the reference model (NRLMSIS). To track the height dependence of the orbit-derived density ratios, we associate each ratio with the drag-weighted average height of the trajectory (the weighting factor is $\rho^M v^3 F$; see equation (3)) [*Emmert et al.*, 2004; *Picone et al.*, 2005].

[18] For objects in elliptical orbits, the effects of drag are concentrated near perigee, and in this case the derived densities correspond to localized regions in latitude and local time. The ratios of the orbit-based effective total mass density to the effective (NRLMSIS) model density reduce such differences between orbital trajectories. As shown below, the orbit-derived density ratios depend more strongly on day of year and perigee altitude than on local time and latitude, suggesting that (on timescales of ~3 days) most of their variability is global in nature [e.g., *Marcos et al.*, 1998]. This view is further strengthened when the ratios from all the objects are analyzed collectively; i.e., they can be viewed as representing the departure of the measured, height-dependent global average density from the corresponding model predictions, insofar as the collection of circular and elliptical orbits sample all latitudes and local times.

[19] The ratios of GUVI-based density values to NRLMSIS values, when averaged over the same time period as the corresponding orbit-based values, similarly capture global variations. This is again because of the filtering that a ratio to NRLMSIS provides and because we compute an average over ~3 days. The need for these filters is more critical with GUVI data, which resolve much finer timescales (~1 min), are more highly localized in latitude, longitude, and altitude, and cover only daytime latitudes less than 60° (to avoid auroral contamination of the dayglow).

[20] To compare the GUVI and drag densities, we first evaluated the GUVI/NRLMSIS ratios at the drag-weighted average height of each object and then averaged the ratios over the same time intervals covered by the drag integrations:

$$\left\langle \frac{\rho^T}{\rho^M} \right\rangle_{\Delta t}^{GUVI} = \frac{1}{n} \sum_{j=1}^{n} \frac{\rho^{GUVI}}{\rho^{MSIS}}\left(z_{sat}, t_j^{GUVI}\right) \tag{6}$$

where z_{sat} is the height associated with the orbit-derived density, the subscript Δt represents the time interval encompassed by t_i and t_k (the epochs of the two element sets used for the orbit-derived density), $t_i \le t_j^{GUVI} \le t_k$, and n is the number of GUVI measurements falling within the time interval.

[21] Figure 1 shows examples of the orbit-derived mass density ratios during 2002, computed using equation (3), and the corresponding GUVI density ratios from equation (6). The drag and average GUVI density ratios track each other quite closely, with both curves showing variations of similar amplitude on timescales greater than about 5 days. Both objects shown in Figure 1 were in elliptical, high-inclination orbits with perigee heights of 400–450 km. The dotted lines in the bottom two panels of Figure 1 indicate that the atmospheric drag experienced by the two objects is fairly localized in latitude and local time. Despite the local time-latitude phase differences between the two objects, the density ratio curves are very similar to each other and to the GUVI curve. Around day 200, for example, object 12388 (right side) is at the same local time as GUVI but at substantially different latitude, whereas object 12138 (left side) is at the same latitude but has a nighttime perigee; nonetheless, the large dip near day 200 is captured by all three curves. This result demonstrates that on ~3 day timescales, the normalized densities primarily represent global variations and that systematic dependences on local time and latitude are comparatively minor.

3. Results

[22] We grouped and averaged the orbit-derived density ratios for the 32 objects listed in Table 1 (27 and 23 objects were still aloft at the beginning of 2003 and 2004, respectively), along with the corresponding GUVI density ratios, into 2-day bins (overlapping at 1-day intervals) and four altitude bands: 200–300, 300–400, 400–500, and 500–

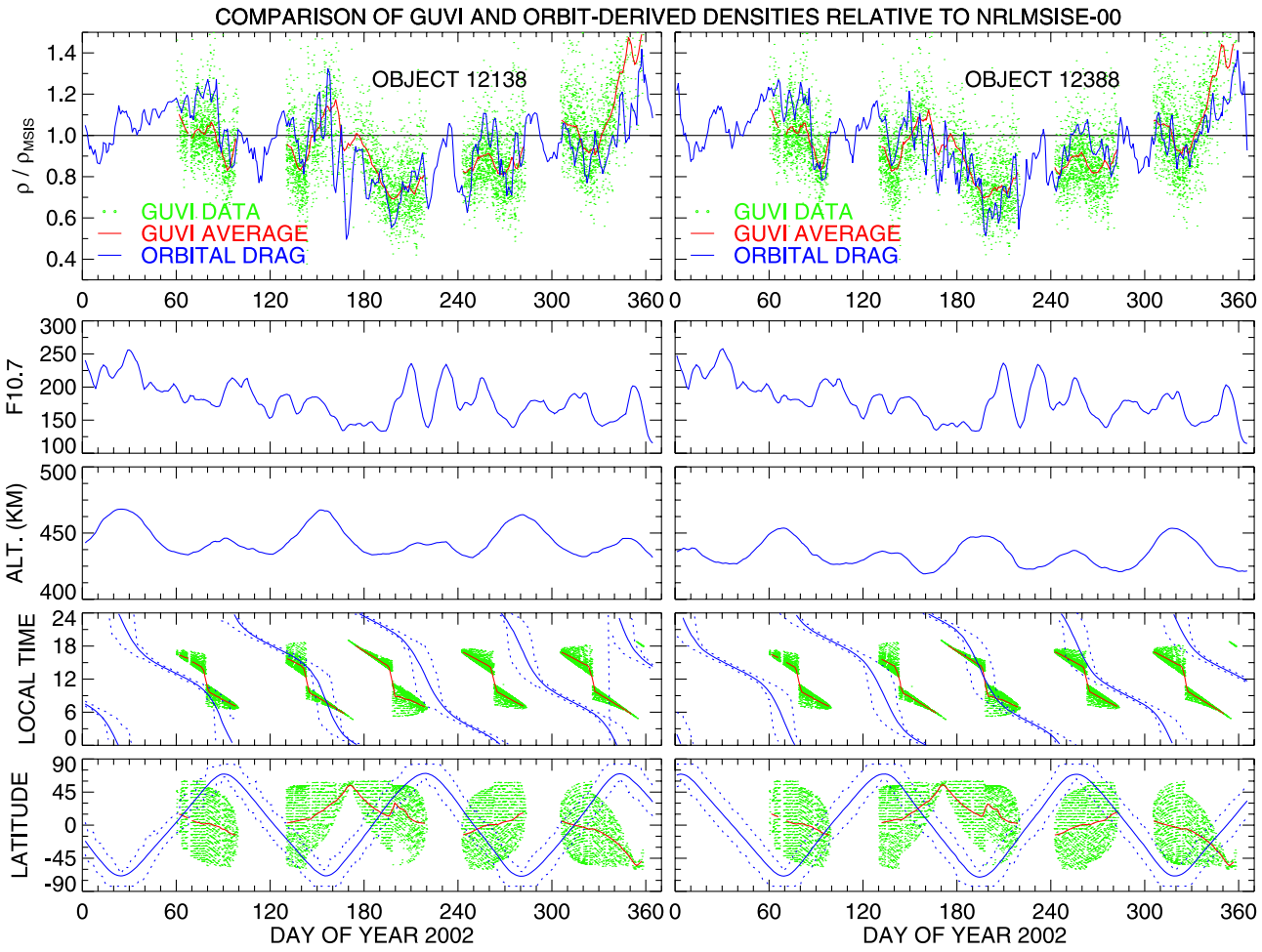

Figure 1. Example of comparison between GUVI and orbit-derived density (relative to NRLMSISE-00) for two specific objects in elliptical orbits. The top panels show orbit-derived density ratios (blue line), GUVI density ratios evaluated at the effective height of the comparison object (green dots), and GUVI density ratios averaged over the time spans covered by the orbital drag integrations (red line). The second row shows the corresponding $F_{10.7}$ indices (averaged over the drag integral time span, about 3 days). The bottom three rows show the drag-weighted average height, local time, and latitude of the two objects (blue lines). Apsidal rotation produces an oscillation in the latitude of perigee, and there is a corresponding variation in the perigee height due to the oblateness of Earth (perigees are higher in the Southern Hemisphere as a result of the third-order zonal harmonic in Earth's gravitational field). The dotted blue lines in the local time and latitude plots indicate the estimated range of values over which 67% of the drag occurred. Also shown in the bottom two rows are the local time and latitude of the GUVI measurements (green dots) and their averages (red line). The point-to-point variations in the unaveraged GUVI data (top panel) are typical of the statistical variation in the data. A full error budget analysis of the GUVI data is in progress and will be presented in a future publication.

600 km. The average altitudes within each of these bins are 260, 352, 442, and 540 km, respectively. Table 2 lists the typical number of objects sampled in each bin; note that fluctuations in the drag-weighted average altitude (e.g., as seen in Figure 1) can affect the sample size of a given 2-day bin.

[23] Figures 2a, 2b, and 2c show the resulting comparisons of drag and GUVI density ratios for 2002, 2003, and 2004, respectively. The agreement is best in the 300–400 km altitude range (which is actually above the 110–300 km range of GUVI radiances used in the inversion; see section 2.2) and during 2002. Both the drag and GUVI ratios appear to contain fluctuations on ~27-day timescales, suggesting that some of the differences between the actual and model atmospheres are associated with solar rotation effects. On shorter timescales (5–15 days), the drag results appear to contain finer structure than the GUVI averages, and this variability increases from 2002 to 2004. This increased variability could be due to greater noise in the drag results during conditions of lower solar extreme ultraviolet (EUV) radiation (the drag "signal" decreases with decreasing density), but the oscillations appear to be coherent among the different height bins (and hence different objects), suggesting that they are a consistent representation of thermospheric variations. Another possibility is that signatures of geomagnetic activity in the drag ratios

Table 2. Typical Sample Size (Number of Objects) of Each Bin

Average Annual Altitude, km	Number of Objects		
	2002	2003	2004
500–600	7	5	4
400–500	18	15	14
300–400	6	3	3
200–300	1	4	2
200–600	32	27	23

(i.e., effects that are not captured by NRLMSIS) feature more prominently in the 2003–2004 data, when the background density is lower. This does not explain why these features are not observed in the GUVI data, but perhaps this variability is less important on the dayside.

[24] The amplitude of the oscillations in both data sets increases with altitude; at the simplest level, this can be understood in terms of exospheric temperature variations around the NRLMSIS predictions. However, the height dependence of the drag density variations is generally stronger than that of the GUVI results, possibly because the GUVI inversions are more constrained to follow the NRLMSIS temperature profiles, as discussed in section 4.

[25] To obtain a more quantitative comparison, we computed statistical characteristics of the two data sets relative to each other and relative to NRLMSIS. We performed this computation in logarithmic space, since the distribution of the log of the ratios is approximately Gaussian, whereas the distribution of the ratios is somewhat skewed owing to its lower bound of zero. Figure 3 shows a log-log scatterplot of the data shown in Figures 2a–2c. The solid red lines show the results of linear regression on the data; if the data were in perfect agreement, they would fall along the dashed black line. The correlation is strongest (0.72) in the 300–400 km bin and is even stronger (0.82) when only the 2002 data are considered (not shown).

[26] Table 3 summarizes the results of our statistical analysis. The second column contains the correlations of the linear fits shown in Figure 3. The third and fourth columns give the relative bias and standard deviation of the GUVI and drag ratios, computed in logarithmic space as follows, and expressed as a percentage:

$$\mathrm{Bias}_{\mathrm{GUVI\text{-}DRAG}} = \exp\left\langle \ln \frac{\rho_{GUVI}/\rho_{MSIS}}{\rho_{DRAG}/\rho_{MSIS}} \right\rangle - 1$$

$$\mathrm{Std\ \ Dev}_{\mathrm{GUVI\text{-}DRAG}} = \exp\left[\mathrm{std\ \ dev}\left(\ln \frac{\rho_{GUVI}/\rho_{MSIS}}{\rho_{DRAG}/\rho_{MSIS}}\right)\right] - 1 \tag{7}$$

where the angular brackets denote the average value. The expressions given in equation (7) are analogous to the mean and standard deviation of the difference between two data sets, except that we are working with ratios, not residuals. The computation consists of (1) transforming the ratios into logarithmic space, (2) performing the usual calculations of the mean and standard deviation, (3) converting back into arithmetic space to obtain the "average" and "scatter" of the ratios, and (4) subtracting 1 to obtain the relative deviation from the zero-bias condition of a ratio of unity.

[27] The fifth and sixth columns in Table 3 give the bias and standard deviation of the GUVI densities relative to NRLMSIS (i.e., the denominators in equation (7) are

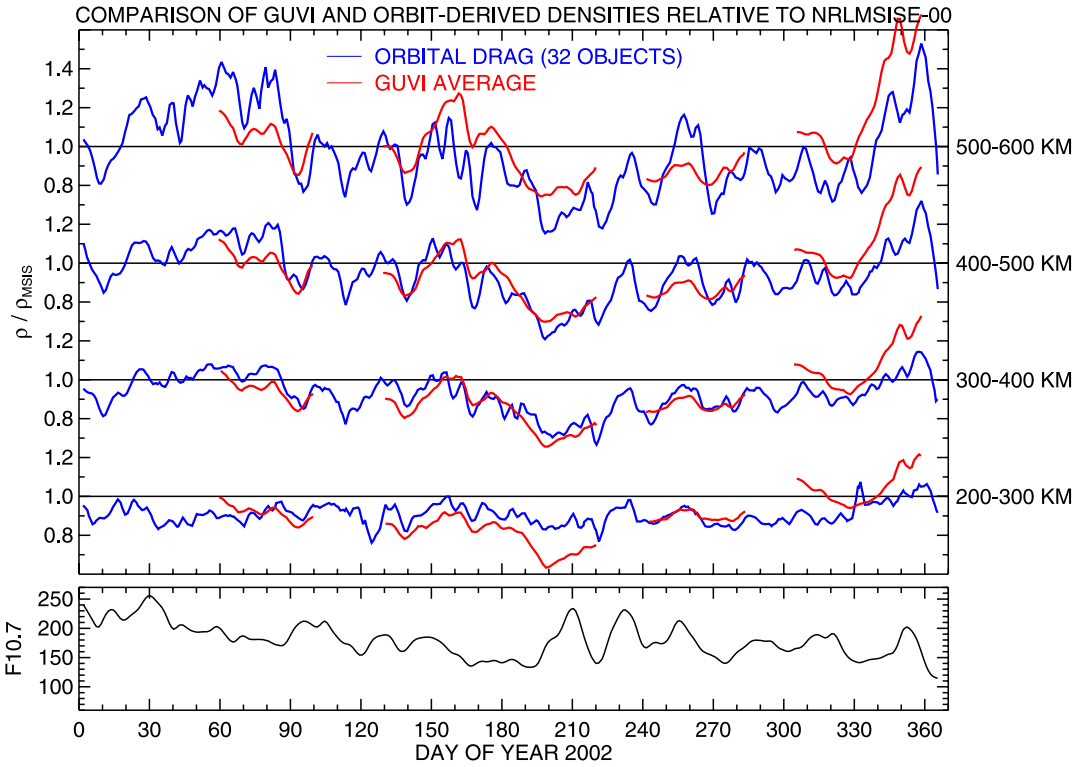

Figure 2a. GUVI and drag density, relative to NRLMSISE-00, during 2002. Results from different objects were averaged together after sorting into the indicated altitude bins. The bottom panel shows the corresponding $F_{10.7}$ indices (averaged over the drag interval time spans, about 3 days).

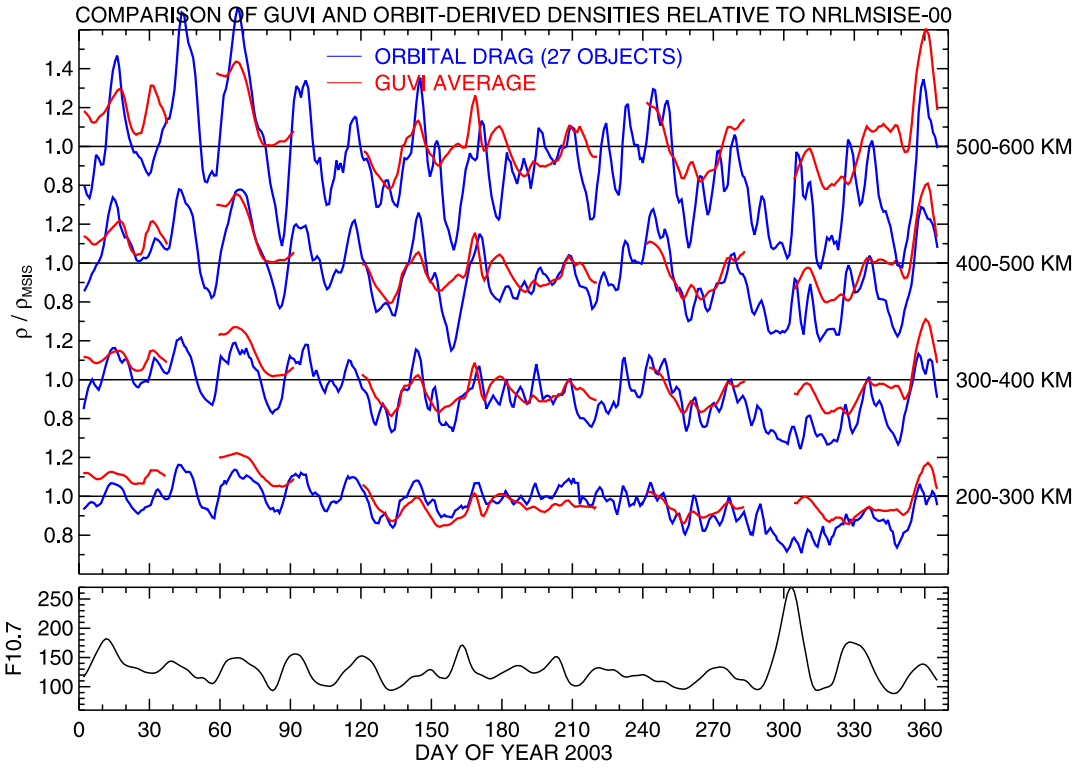

Figure 2b. Same as Figure 2a, for 2003.

omitted), and the last two columns show the corresponding values for the drag densities relative to NRLMSIS; only the time periods covered by the GUVI data were used in these calculations.

[28] The GUVI ratios are 4–14% larger, on average, than the orbit-derived ratios; the bias generally increases with height. Both the GUVI and drag densities are smaller than the NRLMSIS predictions, more so in the case of the drag

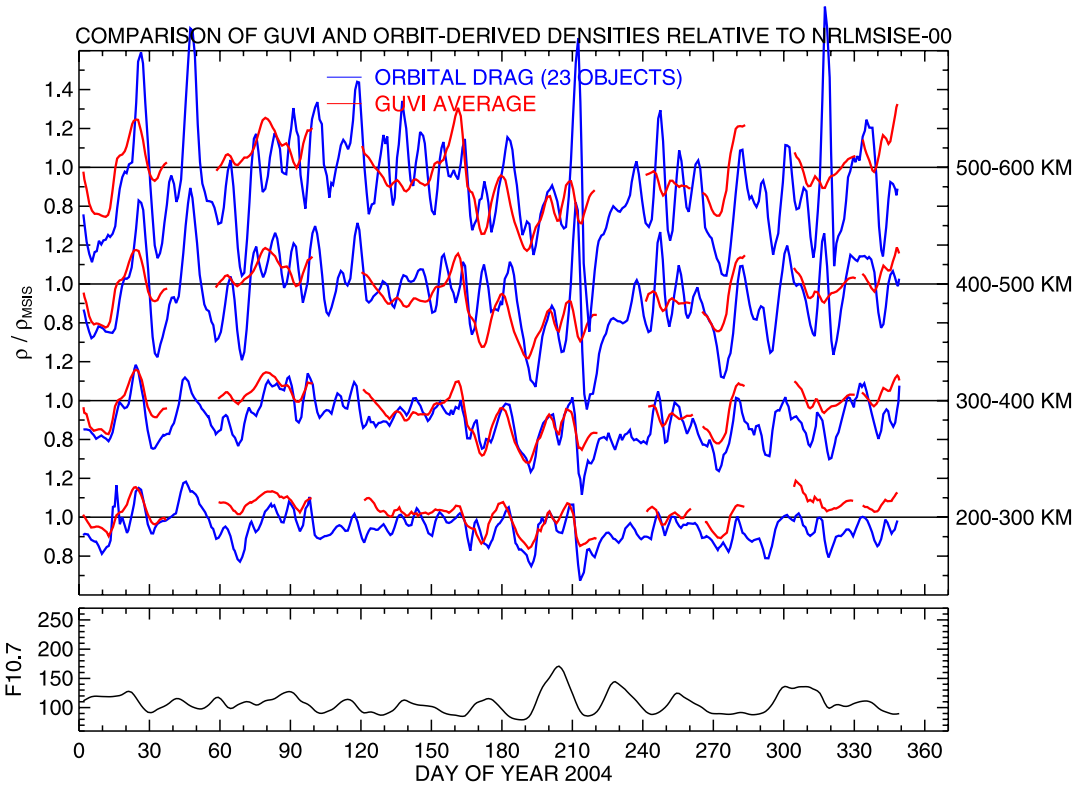

Figure 2c. Same as Figure 2a, for 2004.

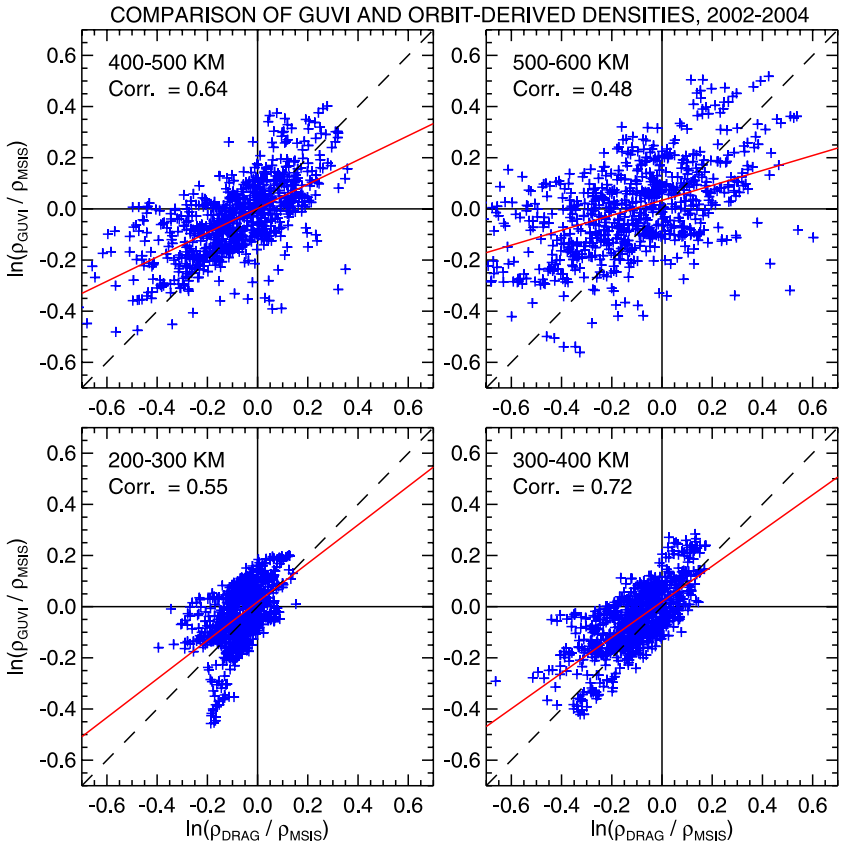

Figure 3. Log-log plot of GUVI density ratios versus corresponding orbit-derived density ratios. All the data from Figures 2a–2c are shown here. The solid red line shows the result of linear regression on the data; the correlation is given in the upper left corner of each panel.

data. This is consistent with the long-term trend results of *Emmert et al.* [2004]: The data underlying NRLMSIS are centered in the early 1980s; given a secular trend of about −3% per decade, one would expect NRLMSIS densities to be about 6% larger than recently observed values, and the GUVI and drag results bracket this estimate.

[29] The variances of the GUVI and drag ratios are comparable in the 200–400 km altitude range, but at higher altitudes the variance of the drag ratios is considerably larger. As discussed in section 4, the total mass density derived from the GUVI profiles is more constrained to follow the NRLMSIS predictions.

[30] Table 4 shows the biases of the GUVI and drag densities, relative to NRLMSIS, for each year. The drag results are more consistent (relative to NRLMSIS) from year to year than the GUVI values. This greater variability may be related to the uncertainties, discussed in section 4, in the GUVI O_2 retrievals.

[31] Figure 4 shows the same density ratios as in Figures 2a–2c but with results from different altitudes superimposed, thereby emphasizing the differences in the altitude dependences of the GUVI and drag results. The spread of the four different curves indicates the magnitude of the height dependence. In most cases, the altitude dependences of the GUVI and drag data have the same sign (generally increasing departures from NRLMSIS with increasing height), with a stronger effect in the drag data. However, near day 200 of 2002, when both data sets show densities that are considerably smaller than NRLMSIS predictions, the orbit-derived ratios decrease with height, whereas the GUVI ratios show a slight increase with height. This behavior is seen more directly in the top panel of Figure 5, which shows results from each object as a function of height. The GUVI results are fairly smooth as a function of height because they effectively represent an average modified NRLMSIS profile; the variations around a smooth profile are due to sampling

Table 3. Statistical Comparison of GUVI and Orbit-Derived Density Ratios, 2002–2004

	GUVI Versus Drag			GUVI Versus NRLMSIS		Drag Versus NRLMSIS	
Altitude, km	Correlation	Bias, %	Std Dev, %	Bias, %	Std Dev, %	Bias, %	Std Dev, %
500–600	0.48	+13.6	28.7	−0.5	18.9	−12.4	32.9
400–500	0.64	+4.8	16.6	−3.9	15.9	−8.3	22.0
300–400	0.72	+5.2	10.0	−5.1	13.4	−9.8	14.0
200–300	0.55	+3.7	10.3	−3.4	12.2	−6.8	8.8

Table 4. Biases of GUVI and Orbit-Derived Density, Relative to NRLMSIS, for Individual Years

	GUVI Versus NRLMSIS Bias, %			Drag Versus NRLMSIS Bias, %		
Altitude, km	2002	2003	2004	2002	2003	2004
500–600	−0.5	+3.7	−4.9	−8.2	−13.5	−14.9
400–500	−5.2	−0.4	−6.4	−7.6	−7.3	−10.1
300–400	−8.9	−1.8	−5.2	−9.0	−8.7	−11.6
200–300	−11.1	−1.4	+1.9	−9.1	−5.2	−6.3

differences in the time periods covered by each comparison object. In a few cases the GUVI altitude dependence is slightly stronger than that of the drag results, and an example of this is shown in the bottom panel of Figure 5.

4. Discussion

[32] Our validation of GUVI retrievals demonstrates that UV remote sensing has advanced from an episodic experimental technique to a reliable method for routinely monitoring thermospheric weather with day-to-day precision greater than that of NRLMSIS and other empirical models. Considering the independence of the drag and UV techniques, it is remarkable that the day-to-day variations of both results track each other so closely and that the average difference is within the experimental accuracy of the drag densities. Nonetheless, distinct systematic differences are evident, and in this section we discuss their possible causes, as well as potential strategies for achieving even better agreement between the two techniques.

[33] As described in section 3, the height dependence of the drag density variations (relative to NRLMSIS) is generally stronger than that of the GUVI results. One likely source of this discrepancy is that GUVI inversions may be overconstrained to follow the NRLMSIS temperature profiles, thereby contributing to discrepancies with the drag altitude profiles. The three NRLMSIS thermospheric temperature parameters (the temperature and its gradient at 120 km, and the exospheric temperature [*Hedin*, 1987]) are all modified by varying the $F_{10.7}$ inputs with a single scaling factor. Thus few of the possible states that can be

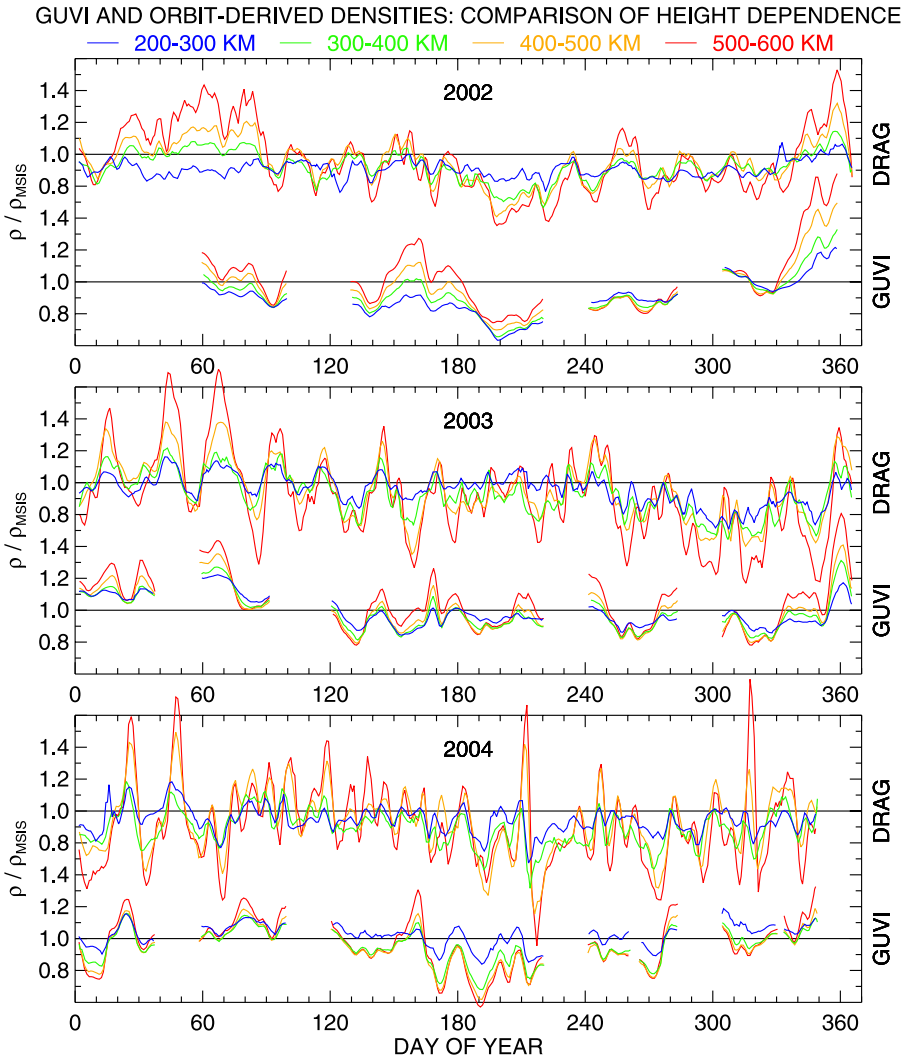

Figure 4. Same data as shown in Figures 2a–2c, but with results from different altitude bins superimposed for (top) 2002, (middle) 2003, and (bottom) 2004. The top portion of each panel shows the orbit-derived densities, and the bottom portion shows the GUVI results.

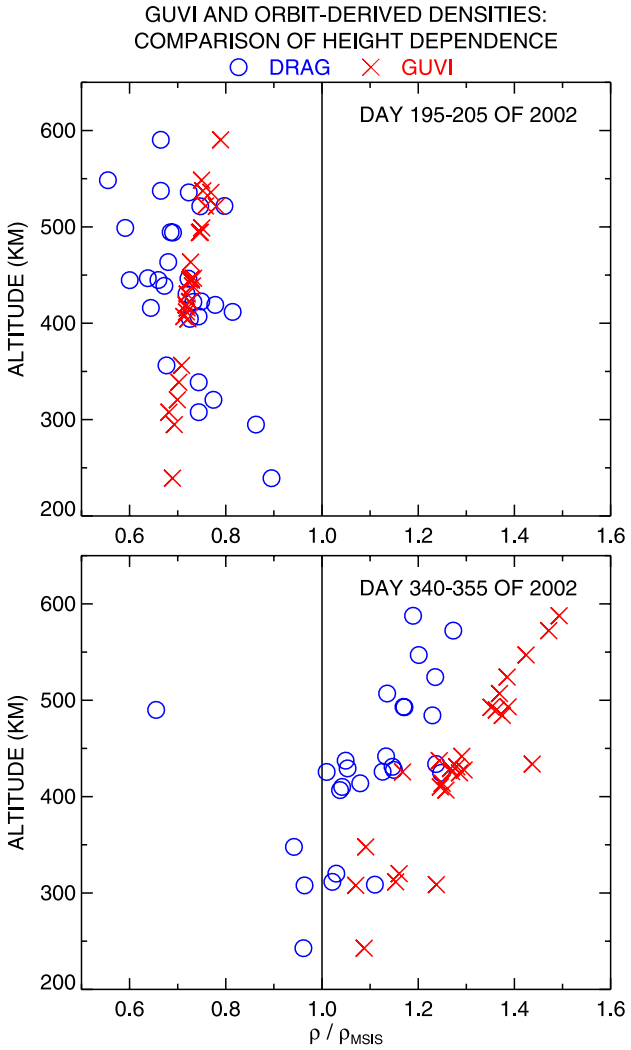

Figure 5. Drag and GUVI density ratios as a function of altitude for two selected periods during 2002: (top) days 195–205 of 2002 and (bottom) days 340–355 of 2002. Each symbol indicates the density ratio from a single object (or the corresponding results from GUVI), averaged over the indicated time period.

represented by the Bates-Walker profile [*Hedin*, 1987], are accessible to the GUVI forward model. In contrast, the drag densities inferred from orbits at different altitudes are not constrained to follow an analytic height profile. Furthermore, in NRLMSIS the lower thermospheric O_2 density has a dependence on $F_{10.7}$ that is unrelated to the $F_{10.7}$ dependence of the temperature parameters, and therefore the $F_{10.7}$ scalar ($f_{F_{10.7}}$ in equation (4)) could compete with the O_2 scalar (f_{O2}) in some inversions. A more flexible inversion can be achieved by scaling the three NRLMSIS temperature parameters directly and independently, rather than simultaneously through the $F_{10.7}$ inputs.

[34] It is also possible that the relative concentrations of O, N_2, and O_2 estimated by the GUVI retrieval procedure may have a bearing on the altitude profile discrepancies. The O_2 densities have large (~40%) uncertainties in the current GUVI inversions, and the values of the O and N_2 scalars depend on the O_2 scalar. This is at least partly because only two spectral features, the OI 135.6 nm and LBHS emissions, are used and are strongly affected by O_2 extinction, which in turn affects the retrievals of O and N_2 densities. An upgraded forward model, incorporating a third emission (N_2 LBH long-wavelength,167.2–181.2 nm) into the inversion, is currently under development and is expected to provide better estimates of O_2 because LBHL is nearly unaffected by O_2 extinction. The upgrade will enable an assessment of the degree to which O_2 extinction influences the retrieved altitude profiles.

[35] Differences in local time sampling may also contribute to (but almost certainly do not fully account for) the weaker height dependence of the GUVI results, since the GUVI data represent daytime conditions, whereas the drag data sample all local times. Although, as noted in section 2.3, the local time dependence of the orbit-derived density ratios is weak compared to the temporal variation of the global mean density, it is possible that small systematic differences between daytime and nighttime scale height departures from NRLMSIS could produce detectable differences in the vertical gradients of the density ratios. Analyzing elliptical orbits only and sorting them by the perigee local time could test this possibility; such an analysis requires more objects with elliptical orbits than we have in our sample.

[36] Finally, both the GUVI and orbital drag values are 30–40% lower than NRLMSIS near days 200–210 of 2002. Evaluation of NRLMSIS with the Mg II (chromospheric) index instead of the $F_{10.7}$ (coronal) index (after statistically normalizing the former to the range of values covered by the latter, treating the daily and 81-day mean values separately) reduces the size of the discrepancy [*Lean et al.*, 2006], suggesting that limitations of $F_{10.7}$ as an EUV irradiance proxy may help explain this feature. Figure 6 illustrates this result, using densities derived from Starshine 3 orbits, relative to NRLMSIS evaluated with $F_{10.7}$ (red curve) and the converted Mg II index (blue curve); the prolonged depletion seen in the $F_{10.7}$ -based ratios is not apparent in the Mg II-based ratios. Further study is needed

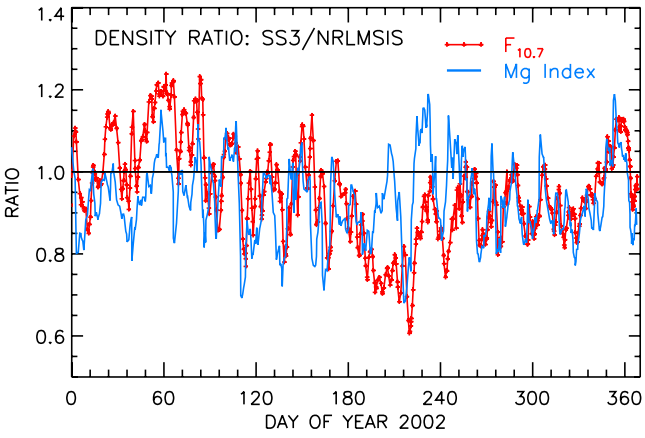

Figure 6. Daily mean density derived from the orbits of Starshine 3 observations, relative to the corresponding NRLMSIS total mass densities. The model densities are evaluated using two different proxies for EUV irradiance, as described by *Lean et al.* [2006]: $F_{10.7}$ (red curve with symbols), and the Mg II chromospheric index (blue curve).

to enhance our understanding of this feature and its relation to EUV irradiance.

5. Summary

[37] Day-to-day variations of dayside GUVI O, N_2, and O_2 densities are in remarkable agreement with global total mass density derived from orbital elements, considering that the two measurement techniques are completely different (one is an inversion of remotely sensed radiation fields and the other is an in situ measurement of a bulk atmospheric property). The overall bias between the two time series is generally within the ~5–10% uncertainty (due to errors in the drag coefficient) of the orbital drag results, and the temporal variations of the two data sets correlate fairly strongly. The agreement is best in the 300–400 km altitude range, where the correlation is 0.72. The height dependence of the GUVI densities is typically weaker than that of the orbit-derived densities, probably as a result of limitations of the parameterization of the GUVI inversion forward model, as well as differences in local time sampling. Both the GUVI and drag results indicate that NRLMSIS over-predicts the total mass density by ~35% near day 200 of 2002, possibly as a result of the limitations of $F_{10.7}$ as an EUV proxy. Future improvements to be pursued include adding a third color to the GUVI inversions to improve our knowledge of the O_2 concentration, increasing the flexibility of the inversion forward model, and restricting the orbital analysis to objects with dayside perigees.

[38] **Acknowledgments.** We thank Liam Healy and Keith Akins at NRL for providing the Naval Space Command orbital elements and NASA's Orbital Information Group for providing the Starshine TLEs. RRM thanks Andrew Stephan for discussions about GUVI retrieval algorithms. This work was supported by the Office of Naval Research, the Defense Meteorological Satellite Program, and NASA.

[39] Arthur Richmond thanks the reviewers for their assistance in evaluating this paper.

References

Bowman, B. R., and K. Moe (2005), Drag Coefficient Variability at 175–500 km from the orbit decay analysis of spheres, paper AAS 2005-257 presented at AAS/AIAA Astrodynamics Specialist Conf., Lake Tahoe, Calif., 7 –11 August .

Carignan, G. R., B. P. Block, J. C. Maurer, A. E. Hedin, C. A. Reber, and N. W. Spencer (1981), The neutral mass spectrometer on Dynamics Explorer B, *Space Sci. Instrum.*, *5*, 429–441.

Champion, K. S. W., and F. A. Marcos (1973), The triaxial-accelerometer system on Atmosphere Explorer, *Radio Sci.*, *8*, 297–303.

Christensen, A. B., et al. (2003), Initial observations with the Global Ultraviolet Imager (GUVI) in the NASA TIMED satellite mission, *J. Geophys. Res.*, *108*(A12), 1451, doi:10.1029/2003JA009918.

Cook, G. E. (1966), Drag coefficients of spherical satellites, *Ann. Geophys.*, *22*, 53–64.

Emmert, J. T., J. M. Picone, J. L. Lean, and S. H. Knowles (2004), Global change in the thermosphere: Compelling evidence of a secular decrease in density, *J. Geophys. Res.*, *109*, A02301, doi:10.1029/2003JA010176.

Hedin, A. E. (1987), MSIS-86 thermospheric model, *J. Geophys Res.*, *92*, 4649–4662.

Lean, J. L., J. M. Picone, and J. T. Emmert (2006), Thermospheric densities derived from spacecraft orbits: 2. Application to the Starshine satellites, *J. Geophys. Res.*, *111*, A04301, doi:10.1029/2005JA011399.

Marcos, F. A., M. J. Kendra, J. M. Griffin, J. N. Bass, D. R. Larson, and J. J. F. Liu (1998), Precision low Earth orbit determination using atmospheric density calibration, in *Astrodynamics 1997: Advances in the Astronautical Sciences*, vol. 97(1), edited by F. Hoots et al., pp. 501–513, Am. Astronaut. Soc., San Diego, Calif.

Marcos, F. A., J. O. Wise, M. J. Kendra, N. J. Grossbard, and B. R. Bowman (2005), Detection of a long-term decrease in thermospheric neutral density, *Geophys. Res. Lett.*, *32*, L04103, doi:10.1029/2004GL021269.

Meier, R. R., and J. M. Picone (1994), Retrieval of absolute thermospheric concentrations from the far UV dayglow: An application of discrete inverse theory, *J. Geophys. Res.*, *99*, 6307–6320.

Meier, R., G. Crowley, D. J. Strickland, A. B. Christensen, L. J. Paxton, D. Morrison, and C. L. Hackert (2005), First look at the 20 November 2003 superstorm with TIMED/GUVI: Comparisons with a thermospheric global circulation model, *J. Geophys. Res.*, *110*, A09S41, doi:10.1029/2004JA010990.

Moe, M. M., S. D. Wallace, and K. Moe (1995), Recommended drag coefficients for aeronomic satellites, in *The Upper Mesosphere and Lower Thermosphere: A Review of Experiment and Theory*, *Geophys. Monogr. Ser.*, vol. 87, edited by R. M. Johnson and T. L. Killeen, pp. 349–356, AGU, Washington, D. C.

Paxton, L. J., et al. (1999), Global ultraviolet imager (GUVI): Measuring composition and energy inputs for the NASA Thermosphere Ionosphere Mesosphere Energetics and Dynamics (TIMED) mission, *Proc. SPIE*, *3756*, 265–276.

Picone, J. M., A. E. Hedin, D. P. Drob, and A. C. Aikin (2002), NRLMSISE-00 empirical model of the atmosphere: Statistical comparisons and scientific issues, *J. Geophys. Res.*, *107*(A12), 1468, doi:10.1029/2002JA009430.

Picone, J. M., J. T. Emmert, and J. L. Lean (2005), Thermospheric densities derived from spacecraft orbits: Accurate processing of two-line element sets, *J. Geophys. Res.*, *110*, A03301, doi:10.1029/2004JA010585.

Schumacher, P. W., and R. A. Glover (1995), Analytic orbit model for U. S. Naval Space Surveillance: An overview, in *Advances in the Astronautical Sciences*, vol. 90, edited by K. T. Alfriend et al., pp. 1893–1912, Univelt, San Diego.

Strickland, D. J., R. R. Meier, R. L. Waltersheid, J. D. Craven, A. B. Christensen, L. J. Paxton, D. Morrison, and G. Crowley (2004), Quiet-time seasonal behavior of the thermosphere seen in the far ultraviolet dayglow, *J. Geophys. Res.*, *109*, A01302, doi:10.1029/2003JA010220.

A. B. Christensen, Northrop Grumman Space Technology, One Space Park, Redondo Beach, CA 90278, USA.

J. T. Emmert, J. L. Lean, and J. M. Picone, E. O. Hulburt Center for Space Research, U.S. Naval Research Laboratory, Code 7643, 4555 Overlook Ave., SW, Washington, DC, USA. (john.emmert@nrl.navy.mil)

R. R. Meier, Department of Physics and Astronomy, George Mason University, 4400 University Drive, Fairfax, VA 22030, USA.